Journal of Materials Research and Technology 35 (2025) 535–544

Contents lists available at ScienceDirect

Journal of Materials Research and Technology

journal homepage: www.elsevier.com/locate/jmrt

Test setup for analyzing the electrical resistance during fatigue loading for metastable austenite AISI 304L and its diffusion-brazed joints

Lukas M. Sauer [a,*], Johannes L. Otto [a], Jonas A. Ziman [b], Peter Starke [b,c], Frank Walther [a]

[a] TU Dortmund University, Chair of Materials Test Engineering (WPT), Dortmund, 44227, Germany
[b] University of Applied Sciences Kaiserslautern, Department of Materials Science & Materials Testing (WWHK), Kaiserslautern, 67659, Germany
[c] Saarland University, Faculty of Natural Sciences and Technology, Saarbrücken, 66123, Germany

ARTICLE INFO

Handling editor: L Murr

Keywords:
In-situ material testing
Electrical resistivity
Direct current potential drop (DCPD)
Microstructural damage
Dislocation density
Electron channeling contrast imaging (ECCI)

ABSTRACT

The measurement of the electrical resistance of specimens based on the established direct current potential drop (DCPD) method is a widely utilized methodology for the detection of damage mechanisms in the field of crack initiation and propagation and change in microstructural details. These include, e.g., dislocation density, void volume fraction, and micro- and macro-cracks. Given the necessity to consider additional factors influencing the electrical resistance, e.g., specimen geometry and temperature, ex-situ measurement techniques are frequently employed through interruption of fatigue testing. However, ex-situ investigations may result in unintended influences, such as changes in contacting, and analyze only discrete states limiting the characterization possibilities and result interpretation. Accordingly, in-situ electrical resistance measurements were employed in this study to characterize the microstructural changes during fatigue with cyclic creeping. To quantify and compensate the effects of geometry, temperature, and deformation-induced austenite-martensite transformation on the electrical resistance during fatigue loading, a complex experimental setup was developed which includes several measurement systems. The combination of strain measurement and potential drop enables a direct transfer of measured strain to electrical resistance. The method was applied and evaluated on high-temperature diffusion-brazed joints with a metastable austenite as base material and Ni-based filler metal. Finally, the change in microstructure was evaluated through electron channeling contrast imaging (ECCI) analyses at different load cycles.

α	Linear resistance temperature coefficient	K^{-1}
A	Cross-section	mm^2
d	Diameter	mm
$\varepsilon_{m,t}$	Total mean strain	–
I	Test current	A
L	Length	mm
L_0	Initial length of extensometer	mm
L_{DCPD}	Length of electrical resistance measurement	mm
$\xi_{vol,\ fit}$	Fitted martensite fraction	%
ρ	Electrical resistivity	$\Omega mm^2/m$
ρ_A	Electrical resistivity of austenite	$\Omega mm^2/m$
ρ_D	Temperature-independent electrical resistivity	$\Omega mm^2/m$
$\rho_{D,\ Austenite}$	Temperature-independent electrical resistivity of austenite	$\Omega mm^2/m$
ρ_M	Electrical resistivity of martensite	$\Omega mm^2/m$
ρ_T	Temperature-dependent electrical resistivity	$\Omega mm^2/m$
R	Electrical resistance	mΩ
R_S	Specimen electrical resistance	mΩ
R_{Shunt}	Shunt resistance	mΩ
T_0	Initial temperature	°C
T_S	Specimen temperature	°C
U	Voltage	mV
U_{Ext}	Voltage drop at extensometer	mV
U_{Shunt}	Voltage drop at shunt	mV

* Corresponding author.
E-mail address: lukas.sauer@tu-dortmund.de (L.M. Sauer).

https://doi.org/10.1016/j.jmrt.2025.01.052
Received 2 December 2024; Accepted 7 January 2025
Available online 8 January 2025

1. Introduction

Electrical resistance measurements with the direct current potential drop (DCPD) setup are established methods for the characterization of microstructural changes [1–3] under various loading conditions. These can be related to the dislocation density [4,5], pore volume fraction [6,7], grain boundary [8,9], precipitates, phase transformation [10] and micro-cracks [11], which obstruct the electrical conduction and led to an influence of the electrical resistance. Nevertheless, it is not possible to separate between various microstructural mechanisms.

In the context of fatigue investigations, electrical resistance measurements are frequently employed to analyze the material reaction in order to identify characteristic loading stages for the purpose of lifetime prediction models [12–14], or to analyze the evolution of microstructure to gain insight into the underlying failure mechanisms [15–17]. In addition to microstructure, geometry and temperature substantially influence the electrical resistance [18,19]. Since the stress ratio of these experiments was set to $R = -1$, the changes in geometry and temperature that occurred during fatigue were minimal and therefore not considered for the electrical resistance. If the stress ratio is $R \neq -1$, these changes must be taken into account [15,20]. In previous fatigue studies, ex-situ measurements were performed after different lifetime intervals, as these methods allows a simple measurement of the electrical resistance and the geometry and preclude the occurrence of fatigue-induced heating [15,21,20]. However, ex-situ investigations may be susceptible to unintended influences resulting from interruption, which could potentially lead to inaccurate measurements. Furthermore, the development between the selected intervals cannot be determined, which suggests that the number of intervals should be as high as possible. However, this would lead to a greater experimental effort and a higher number of influences. In contrast, in-situ investigations provide the potential for continuous measurement during the fatigue test.

Therefore, this study presents a method for the evaluation of microstructural changes during fatigue by using in-situ electrical resistance measurement. Therefore, the established direct current potential drop setup was employed, which uses the four-terminal setting [18]. Thereby, current input and potential drop are accomplished to separated cables, eliminating the effects of resistance in the wiring and contact points [18]. The utilization of direct current (DC) in contrast to alternating current (AC) enables the analyzation of the entire cross-section of the specimen, while AC is concentrated on the surface area [18].

In order to compensate the previously mentioned influences of geometry and temperature on the electrical resistance, a complex in-situ measurement and sensor setup was developed. For this purpose, a combination of extensometer and potential drop was developed, which allows the reliable transfer of the strain, measured by the extensometer, to the length of the electrical resistance measurement during fatigue. Since geometrical and thermal influences were compensated, the microstructural changes can be evaluated and validated based on microscopic analyses. Fig. 1 illustrates schematically the described method used in this study.

The proposed method was evaluated on high-temperature brazed austenitic steel joints. The high-temperature vacuum brazing of metastable austenitic alloys is an established process for joining highly stressed structures with specific joint points [22,23]. The high degree of design flexibility allows for the integration of both thin-walled structures and full-surface components. Due to the high mechanical, thermal, and corrosive properties of the material, metastable austenitic steels are often utilized as base material for brazing applications, in conjunction with Ni-based filler-metals with a solidus temperature exceeding 800 °C. During the brazing process, the brazed joints are subjected to high brazing temperatures (1160 °C) in conjunction with extended holding times (approx. 60 min), which result in a significant microstructural change of the base material e.g., a reduction in the dislocation density, which has a significant impact on the mechanical properties of the brazed joint [24,25]. Due to the application in highly loaded structural components, cyclic loading results in further microstructural changes, which includes the formation and migration of dislocations, pore formation and deformation, and the growth of micro-cracks, which result in a significant influence on the mechanical, thermal and corrosive properties. The assessment of the microstructural change evolution resulting from fatigue loading through non-destructive testing (NDT) methods represents an important aspect of the optimization of brazed joints.

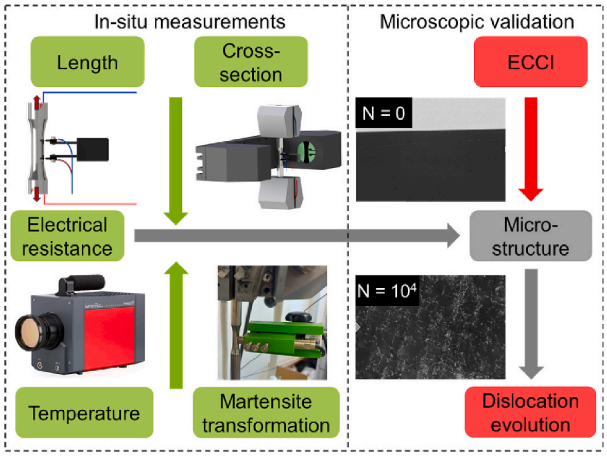

Fig. 1. Schematic description of this study.

2. Experimental details

2.1. Material

The material used is the metastable austenitic stainless steel AISI 304L (X2CrNi18-9, 1.4307) in the form of cold-drawn bar material of 16 mm diameter with an average grain size before brazing of about 60 µm. The cold-drawn base material has high cold strength, which is largely reduced by the brazing process [26]. An experimental Ni-based filler metal was used in form of amorphous foil with a thickness of about 45 µm, which was produced by melt spinning on a fast-rotating copper disk. The chemical composition of the base material and filler material as well as the solidus and liquidus temperatures determined by differential scanning calorimetry (DSC) are shown in Table 1.

During the high-temperature vacuum brazing process, the specimens were heated to the brazing temperature of 1160 °C. Holding stages were added at 800 °C and 900 °C to improve the vacuum quality and to homogenize the specimen temperature. The brazing temperature was then held for 60 min, followed by cooling under vacuum and later through nitrogen inflation. Fig. 2 shows the time-temperature curve of the brazing process. Fatigue specimens with a test diameter of 8 mm, a gauge length of 12.5 mm, and a clamping diameter of 12 mm were turned from the brazed joints, illustrated in Fig. 3.

The specimens' microstructure after the brazing process was analyzed using scanning electron microscopy (SEM) with backscattered electrons (BSE) and electron backscatter diffraction (EBSD) techniques. As can be seen in Fig. 3, the specimen center displays by BSE a brighter zone due to the high nickel proportion, which is the so-called of isothermal solidification zone, that has solidified due to diffusion processes at brazing temperature [27,28]. In the so-called diffusion zone, the (grain boundary-) diffusion of the small and light melting point depressing element boron, resulted in the formation of brittle chromium-rich borides on the austenite grain boundaries. Further detailed descriptions of the formation of the brittle phases and the influence on fatigue behavior can be found here 27,29,30. The total width of the brazing seam (combined diffusion zones and solidification zone width) is approx. 190 µm, thus representing about 2 % of the

Table 1
– Chemical compositions and melting range of the base material and filler metal.

	Chemical composition [wt. %]								Melting range [°C]	
Alloy	Fe	Ni	Cr	C	Si	Mn	Mo	B	$T_{Solidus}$	$T_{Liquidus}$
AISI 304L	Bal.	8.08	18.34	0.02	0.02	1.64	0.33	–	1400	~1450
Ni-filler	4	Bal.	15	–	7.5	–	0	1.5	1060	1122

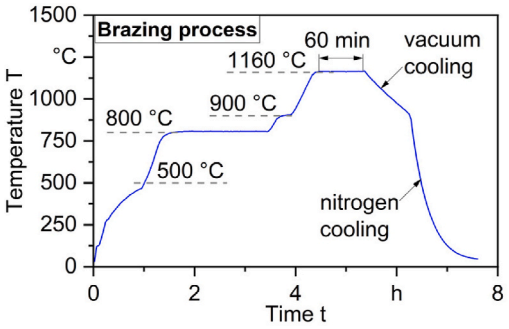

Fig. 2. Time-temperature curve of the brazing process.

measurement length L_0 from the extensometer. Consequently, the majority is measured in the base material, approx. 98 %. Therefore, the effect of the brazing seam on the electrical resistance was low. But the high temperature at the holding time during the brazing process resulted in a notable increase in grain size, with partial abnormal grain size distribution. Furthermore, the brazing process resulted in a significant reduction in dislocation density. The microstructure changes, especially the grain size and dislocation density, lead to an increase of ductility and a reduction of the ultimate tensile strength [27].

2.2. Experimental setup

The fatigue tests were performed with a uniaxial servohydraulic testing system, Instron 8801, with a maximum force of ±100 kN. The testing was conducted under uniaxial load with a constant stress

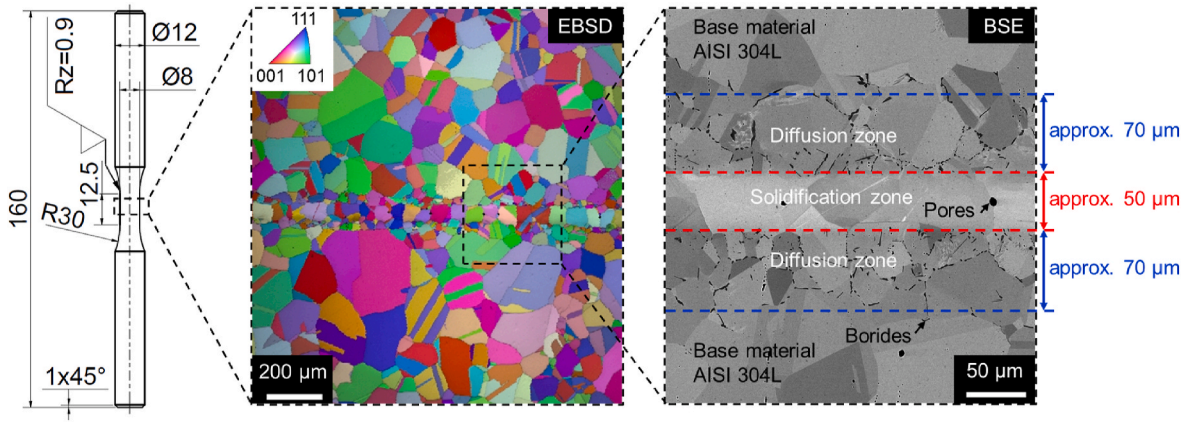

Fig. 3. – Specimen geometry and microstructure after the brazing process.

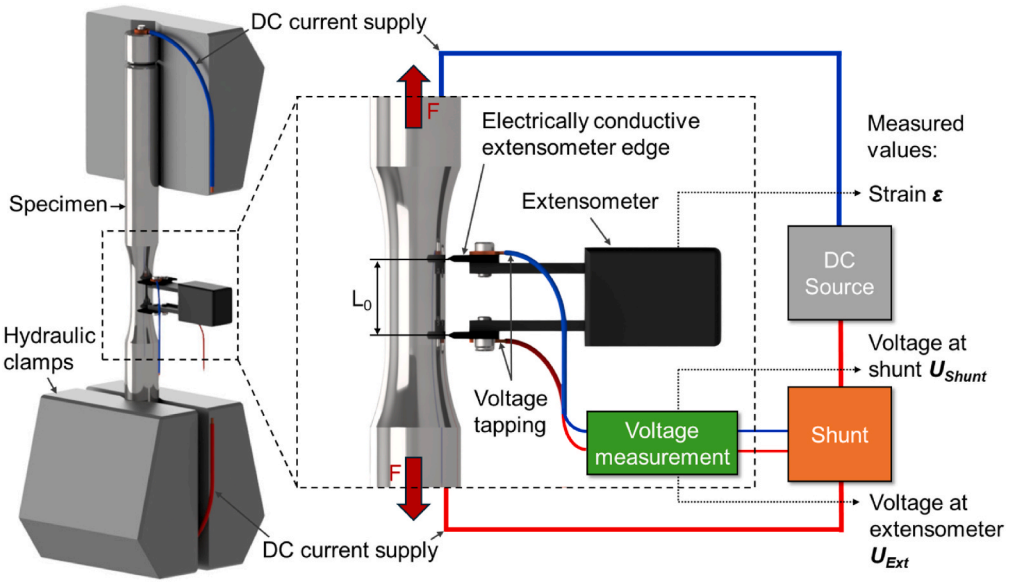

Fig. 4. New direct current potential drop (DCPD) setup coupled with strain measurement of the extensometer [31].

amplitude and a stress ratio of $R = 0.1$ (tension-tension range). The test frequency was $f = 10$ Hz. Various in-situ measurement systems were employed, as shown in Figs. 4 and 5.

2.2.1. In-situ geometry measurement

The strain ε was measured through an extensometer with a measuring length of approx. $L_0 = 10$ mm. The total mean strain $\varepsilon_{m,t}$ and plastic strain amplitude $\varepsilon_{a,p}$ were determined through the stress-strain hysteresis. For the measurement of the diameter d a 2-dimensional optical micrometer was used, which was attached to the servohydraulic testing system.

2.2.2. In-situ temperature measurement

The specimen temperature T_S was measured by eight type K thermocouples, six of them were applied to the specimen. To validate the point measurement by the thermocouples, the spatial temperature distribution was also determined for two separated fatigue tests with the high-speed thermography system InfraTec Image IR 8800. The specimen were coated with a black lacquer to obtain a defined emissivity.

2.2.3. In-situ electrical resistance measurement

The electrical resistance of the specimen was measured by using the direct current potential drop (DCPD) setup. The current was introduced through the clamping jaws of the testing system. Therefore, a Sorensen 8AS2 direct current was used. The test current I was measured trough a shunt resistor integrated into the circuit. By applying a voltage tap across the shunt, the test current can be calculated according to Ohm's law, Equation (1) [18]. The schema of the electrical resistance measurement is shown in Fig. 4.

$$I = \frac{U_{Shunt}}{R_{Shunt}} \tag{1}$$

To measure the electrical resistance R_S, a new method was developed to tap the voltage via the electrically conductive cutting edges of the extensometer, which were connected with cables to the voltage measurement [31]. The voltage tap via extensometer enables the measurement of the electrical resistance locally in the gauge length without the need for additional welding or brazing of cables, which can unintendedly affect the microstructure. Since strain measurement and voltage drop are locally combined, the total mean strain $\varepsilon_{m,t}$, can be used to calculate the length of electrical resistance measurement L_{DCPD}, see Equation (2).

$$L_{DCPD} = L_0 \cdot (1 + \varepsilon_{m,t}) \tag{2}$$

2.2.4. Martensite fraction

In case of the metastable austenite AISI 304L, deformation leads to an induced transformation of paramagnetic austenite to ferromagnetic α′-martensite [32]. As α′-martensite has a lower electrical resistivity than austenite, an increase in the α′-martensite fraction ξ_{vol} results in a reduction of the combined electrical resistivity ρ, independent of the other microstructural changes [33]. Evaluation of microstructural changes by the electrical resistivity therefore requires consideration of the α′-martensite fraction ξ_{vol}.

A feritscope FMP30 by Helmut Fischer was applied to measure the α′-martensite fraction $\xi_{vol,measured}$ during fatigue. According to the manufacturer, the use of a correction factor is necessary when measuring round samples. The manufacturer provides a method for calculating the correction factor [34]. In this study, the correction factor was determined through interpolation based on the measured α′-martensite fraction and the diameter of the sample.

2.2.5. Combination of measurement systems

The combination of extensometer, optical micrometer, thermocouples, voltage measurements at extensometer and shunt, and feritscope measurements, along with synchronous data acquisition, enabled the measurement of all variables relevant to the separation of geometrical, thermal and martensite transformational influences on the electrical resistance, to evaluated the microstructure during fatigue. Fig. 5 shows the combined experimental setup.

2.3. Microstructure analyses

For microstructural analyses, specimens were fatigued up to a defined fatigue state and metallographic cross-sections were made from the specimens. Microstructural changes were studied in the solidification zone of the brazed joint and in the base material at a distance of at least 100 µm from the brazed joint to avoid misinterpretations due to the influence of diffusion effects.

Of particular interest to this study was the development of dislocations, as it is a major factor influencing electrical resistivity, along with austenite-martensite transformation [32]. In addition to the time-consuming and equipment-demanding transmission electron microscopy (TEM), the electron-channelling contrast imaging (ECCI) method is useful for analysing dislocations [35]. It is based on the

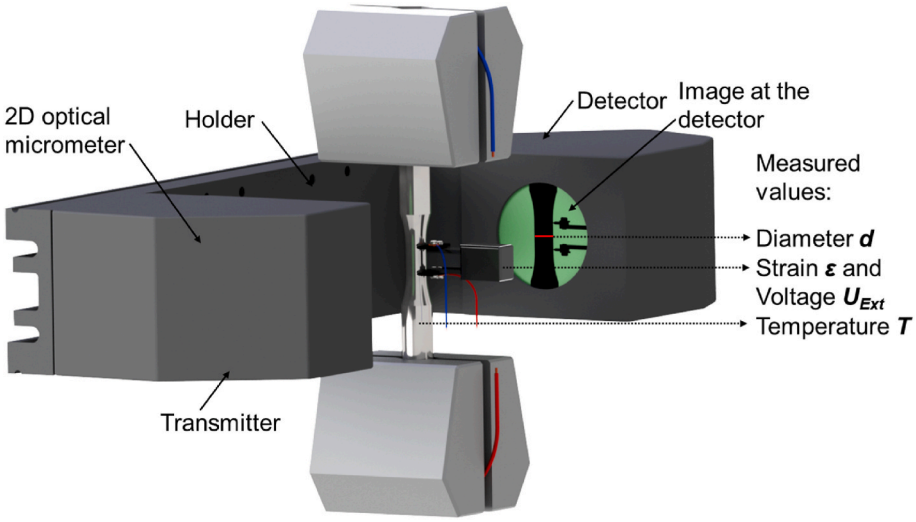

Fig. 5. Combined measurement of extensometer, direct current potential drop (DCPD), thermocouples (not shown here) and optical micrometer for comprehensive in-situ measurement during the fatigue tests.

interaction of an electron beam with the periodic lattice of a crystal. When the electron beam hits the material, the electrons are channelled along the crystal lattice planes, resulting in so-called channelling electron scattering. The intensity of the backscattered electrons depends on the angle of the electron beam relative to the lattice planes. Therefore, the tilt of the specimen and the grain orientation are important. This angle dependence of the electron intensity enables to generate a high contrast between lattice structure and lattice defects. Thus, ECCI enables the visualization of defects such as dislocations, stacking faults and grain boundaries. To achieve maximum image quality, the specimen tilt can be calculated based on additional electron backscatter diffraction (EBSD) [35]; however, in this study suitable grain orientations were identified in the microstructure for different tilts.

3. Results and discussion

3.1. Electrical resistance during fatigue

The electrical resistance in the gauge length R_S was calculated according to Equation (3) from the voltage drop at the extensometer U_{Ext} and the test current I. During the fatigue test, a significant increase in electrical resistance R_S can be observed, Fig. 6 b). In the following, several factors influencing the electrical resistance during the fatigue test are considered in order to determine the temperature-dependent electrical resistivity of the austenite, from which the evolution of the microstructural changes was evaluated.

$$R_S = \frac{U_{Ext}}{I} = \frac{U_{Ext} \cdot R_{Shunt}}{U_{Shunt}} \tag{3}$$

3.1.1. Geometric influence

Fig. 6 a) shows the comparison of plastic strain amplitude $\varepsilon_{a,p}$ and total mean strain $\varepsilon_{m,t}$ during fatigue. The significant increase in the total mean strain shows the cyclic creeping of the material. The plastic strain amplitude shows a high peak at the beginning of the fatigue test (related to initial work hardening). In the further course cyclic softening can be seen. Since the total mean strain is significantly higher than the plastic strain amplitude, cyclic creeping is the dominating mechanism. Therefore, the total mean strain was only used for the following evaluation.

According to Pouillet's law, the influence of geometry on the electrical resistance can be described by Equation (4) and Equation (5) through the electrical resistivity ρ and the geometry of the specimen, namely the length L and cross-section A [36]. Consequently, the electrical resistivity is independent from the geometry and can be used to compensate the influence of geometrical changes on the electrical resistance [36].

Therefore, the cross-section A was determined through actual specimen diameter d. For the determination of the length electrical resistance measurement L_{DCPD}, the total mean strain $\varepsilon_{m,t}$ was measured through the extensometer. As a result, the measured length of the extensometer is identical to the length of the electrical resistance measurement L_{DCPD}, $\varepsilon_{m,t}$. Accordingly, the electrical resistivity ρ during fatigue was calculated according to Equation (5), see Fig. 7. As a result of the high maximum stress and the high ductility of the base material, the beginning of the fatigue test shows a significant increase in total mean strain and length and reduction in diameter. In contrast to the electrical resistance, the electrical resistivity remains in the same range. Consequently, the significant increase of the electrical resistance can be explained by the geometrical influences.

$$R = \rho \frac{L}{A} \tag{4}$$

$$\rho = \frac{R_S \cdot \pi \cdot d^2/4}{L_0 \cdot (1 + \varepsilon_{m,t})} \tag{5}$$

3.1.2. Comparison with welded contacting

In the newly developed experimental setup, the edges of the extensometer are attached to the specimen via bands. In contrast to fixed contacts, this leads to a possibility of a transient alteration in the contact situation, such as the loosening of the connection between specimen and extensometer, which could potentially influence the precision of the measurement. In order to compare the newly developed experimental setup with established fixed contacting methods, two specimens were provided with laser welded contacts at distances of 10 mm, corresponding to the measuring range L_0 of the extensometer. During fatigue the electrical resistance was measured with both the fixed laser welded contacts and the extensometer. For both contact methods, the electrical resistivity ρ was calculated according to Equation (5), see Fig. 8, and compared with the electrical resistivity of a specimen without laser welded contacts.

The scattering of both contacting methods is comparable. The trend is also comparable, with the laser welded connection exhibiting a more pronounced increase in electrical resistivity prior to failure, attributed the fracture initiate at welded contact point, leading to a significant decrease in the lifetime of approx. 90%. In case of changes in the contact situation during fatigue, an increase in the scattering is anticipated. Since scattering and trend of both contacting is comparable, the potential drop via extensometer is reliable method in this study.

3.1.3. Thermic influence

In the gauge length, a nearly constant temperature distribution for different numbers of cycles was determined through thermography, shown in Fig. 9. Also, the thermography and thermocouple in-situ temperature measurements during fatigue is comparable, shown in Fig. 10 a). Accordingly, thermocouple temperature measurement is a reliable method in the study and can be used to characterize the gauge length temperature.

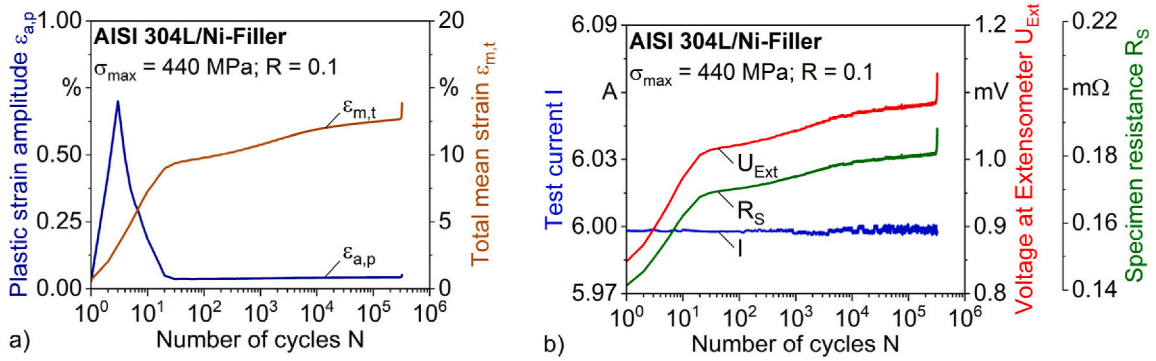

Fig. 6. – a): Comparison of plastic strain amplitude $\varepsilon_{a,p}$ and total mean strain $\varepsilon_{m,t}$ during fatigue; b): Voltage at extensometer U_{Ext}, test current I and electrical resistance of specimen R_S during the fatigue test.

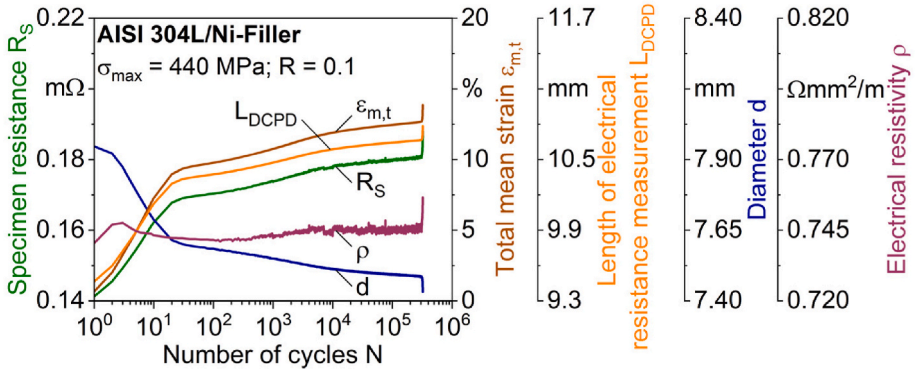

Fig. 7. – Electrical resistance of specimen R_S, the total mean strain $\varepsilon_{m,t}$ length of electrical resistance measurement L_{DCPD}, diameter d and determined electrical resistivity ρ during the fatigue test.

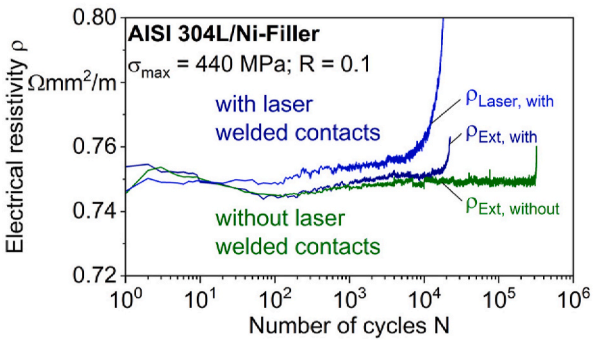

Fig. 8. – Comparison between contacting via extensometer and laser welded contacts.

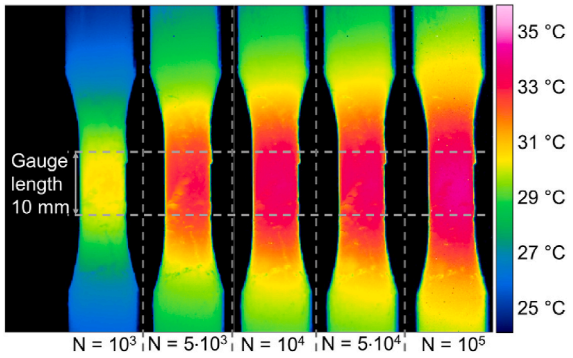

Fig. 9. – Spatial temperature distribution for different lifetime stages with marked test area.

The thermal influence on the electrical resistance R can be described by the Matthiesen rule, where the electrical resistivity ρ is divided into a temperature-dependent ρ_T and a temperature-independent ρ_D portion [19], see Equation (6). The temperature independent portion ρ_D depends on the defect density and is therefore used to evaluate the microstructure. For applications at room temperature, the temperature-dependent portion can be simplified to a linear relationship, see Equation (7), with the linear resistance temperature coefficient α, the specimen and refence T_S and T_0 and the electrical resistivity at reference temperature ρ_0. The linear resistance temperature coefficient α was determined to $\alpha = 1.231 \pm 0.116\ K^{-1}$ for the brazed joint by heating a load-free specimen while measuring the temperature and electrical resistance. Therefore, the temperature-independent ρ_D portion during fatigue can be calculated according to Equation (8), see Fig. 10b).

$$\rho = \rho_D + \rho_T \tag{6}$$

$$\rho_T = \rho_0 \cdot (1 + \alpha \cdot (T_S - T_0)) \tag{7}$$

$$\rho_D = \rho - \rho_0 \cdot (1 + \alpha \cdot (T_S - T_0)) \tag{8}$$

3.1.4. Martensitic transformation influence

If several conductive phases are present in a cross-section, the resulting electrical resistivity can be assumed by different ways [37,38]. The simplest models are based on either a series or parallel connection [34]. For the real microstructure, small amounts of martensite surrounded by austenite, the resulting electrical resistivity can calculate through the Reynolds model, see Equation (9) [38].

The initial electrical resistivity of the martensite ρ_M varies significantly in the literature depending on the chemical composition and temperature [33,37,38]. The values for AISI 304L at room temperature were determined partly through the use of linear interpolation of the chemical composition and the temperature. The values ranged from 0.35 $\Omega mm^2/m$ to 0.5 $\Omega mm^2/m$. Since [33] and [367 provided a value of 0.35 $\Omega mm^2/m$, this electrical resistivity of the martensite was used in the following analysis. The initial electrical resistivity of the austenite is for AISI 304L at $\rho_A = 0.74\ \Omega mm^2/m$. Since the α′-martensite fraction is low, only the resistance of the austenite was considered for further evaluation, which can be calculated from the temperature-independent total resistance and the α′-martensite fraction. Fig. 10 b) shows the determined course of temperature-independent electrical resistivity of the austenite $\rho_{D,\ Austenite}$.

$$\rho = \frac{\rho_A(\rho_A + 2\rho_M)}{(1 + 3\xi_{vol})\rho_A + (2 - 3\xi_{vol})\rho_M} \tag{9}$$

3.2. Discussion of the electrical resistance

When determining the temperature-independent electrical resistivity of austenite $\rho_{D,\ Austenite}$, the influences of geometry, temperature, and martensite were considered. and are no longer included in the signal. Consequently, the microstructural changes during fatigue can be evaluated.

During fatigue, an increase in the temperature-independent electrical resistivity of the austenite can be observed in the first three cycles, which is fully reversed after $N = 10^2$ cycles. One possible reason for this is a significant increase in the dislocation density within the initial cycles. Due to the increased grain size, subsequent migration of dislocations occurs towards the grain boundaries. At these boundaries, the electrical resistivity is less significantly influenced by the dislocations, resulting in a reduction in the electrical resistivity. Another possible reason could be the significant plasticization of the material, which, as shown in Fig. 6, also occurs in the first three cycles. Resolution errors

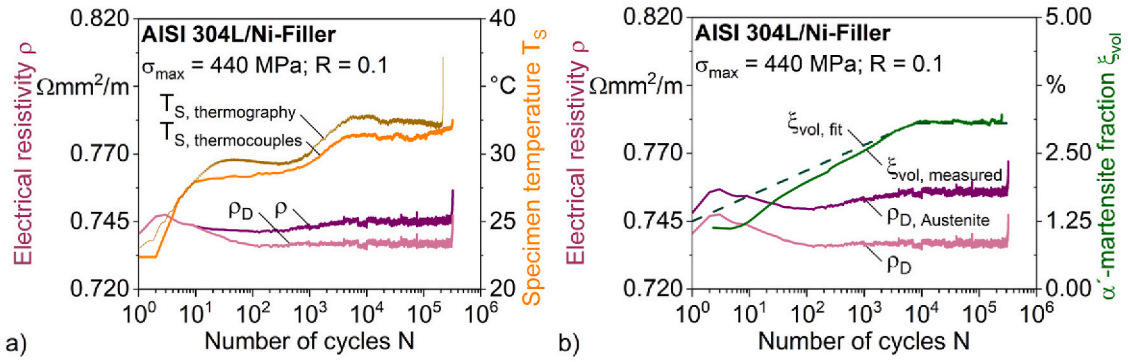

Fig. 10. – a): Electrical resistivity ρ, temperature-independent electrical resistivity ρ_D, specimen temperature $T_{S,\ thermocouples}$ measured with thermocouples and with thermography $T_{S,\ thermography}$ during fatigue; b) Temperature-independent electrical resistivity ρ_D, temperature-independent electrical resistivity of the austenite $\rho_{D,\ Austenite}$, measured and fitted α′-martensite fraction $\xi_{vol,\ measured}$, $\xi_{vol,fit}$ during fatigue.

due to the test frequency of $f = 10$ Hz could also influence the measurement and determination, as the first three cycles are completed in 0.3 s. To improve the resolution of the initial cycles, two separate fatigue tests were conducted at a test frequency of $f = 0.1$ Hz (10 s per cycle instead of 0.1 s per cycle). The remaining experimental parameters and measurement systems were kept constant. Consequently, the temperature-independent electrical resistivity of the austenite $\rho_{D,\ Austenite}$ was also determined for $f = 0.1$ Hz using the previous method, see Fig. 11. Since no notable difference between the temperature-independent electrical resistivity of the austenite $\rho_{D,\ Austenite}$ at high ($f = 10$ Hz) and low ($f = 0.1$ Hz) frequencies was observed, it is assumed that the resolution at a test frequency of $f = 10$ Hz is high enough.

Furthermore, temperature-independent electrical resistivity of the austenite $\rho_{D,\ Austenite}$ increases continuously throughout the fatigue test until it reaches a level close to a constant value after $N = 10^4$ cycles. A potential cause could be a further continues increase in the dislocation density. Subsequently, ECCI investigations are employed for the purpose of validating the increase of dislocation density and dislocation movement at different number of cycles.

3.3. Microstructural defect analysis

To validate the interpretation of the electrical resistance, the change in the dislocation structure was analyzed. Therefore, ECCI was used in the SEM on cross sections of the specimens before, after $N = 10$ cycles and after $N = 10^4$ cycles at $\sigma_{max} = 440$ MPa. Fig. 12 shows the evolution of the dislocation structure and density based on the ECCI scans in the base material and in the solidification zone of the brazing seam.

Due to the high grain size and low dislocation density before fatigue, which were caused by the brazing process, this qualitative method was particularly suitable. The development of the dislocation structure in polycrystalline austenite is always influenced by the grain orientation in loading direction [39], which was not considered in this study. Instead, several different grains were investigated and the scans shown in Fig. 12 are examples of the typical development.

As can be seen in Fig. 12 a), almost no superordinate dislocation structures could be found in the base material by means of ECCI before fatigue, even at different grain orientations and different tilts of the specimen. In the solidification zone in Fig. 12 d), individual dislocations could be observed before fatigue, as well as a few stacking faults. Since stacking faults are planar defects that are aligned along a particular slip or crystal plane, they appear with good contrast as straight lines with partial interruptions, as can be seen in Ref. [40].

This difference can be explained by the fact that during cooling after the brazing process, residual stresses arise inside the brazing seam due to different thermal expansion coefficients between the solidification zone and the base material [25], which already influence the crystal structure. As can be seen in Fig. 12 b), individual dislocations after $N = 10$ cycles can now also be seen in the base material in the entire grain, which begin to form clusters at the grain boundaries. In addition, an increased number of stacking faults were observed. The same tendency can be observed in the solidification zone in Fig. 12 e), but with a higher overall dislocation density and a few dislocation clusters inside the grain. After $N = 10^4$ cycles, a further significant increase in dislocation density was observed, as can be seen in Fig. 12 c) and 12 f). Pronounced clusters can be seen over the entire grains. With further fatigue, it can be assumed that the dislocations will accumulate and structures with

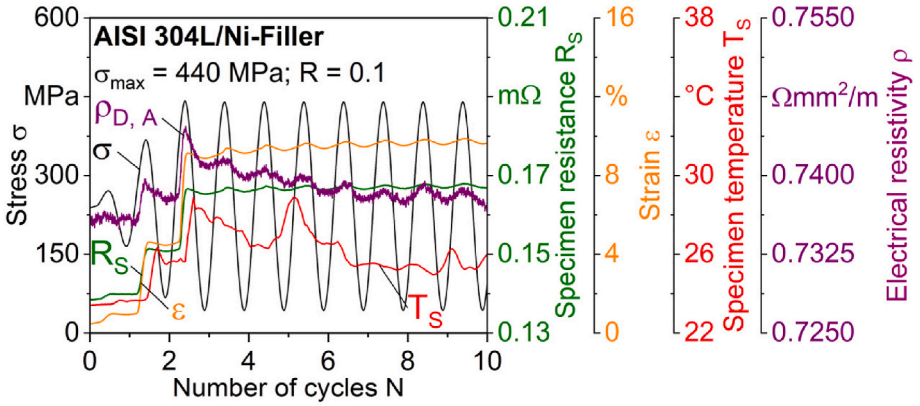

Fig. 11. – Measured strain ε, temperature T_S, electrical resistance R_S and determined temperature-independent electrical resistivity of the austenite $\rho_{D,\ Austenite}$ for the first 10 cycles at a test frequency of $f = 0.1$ Hz.

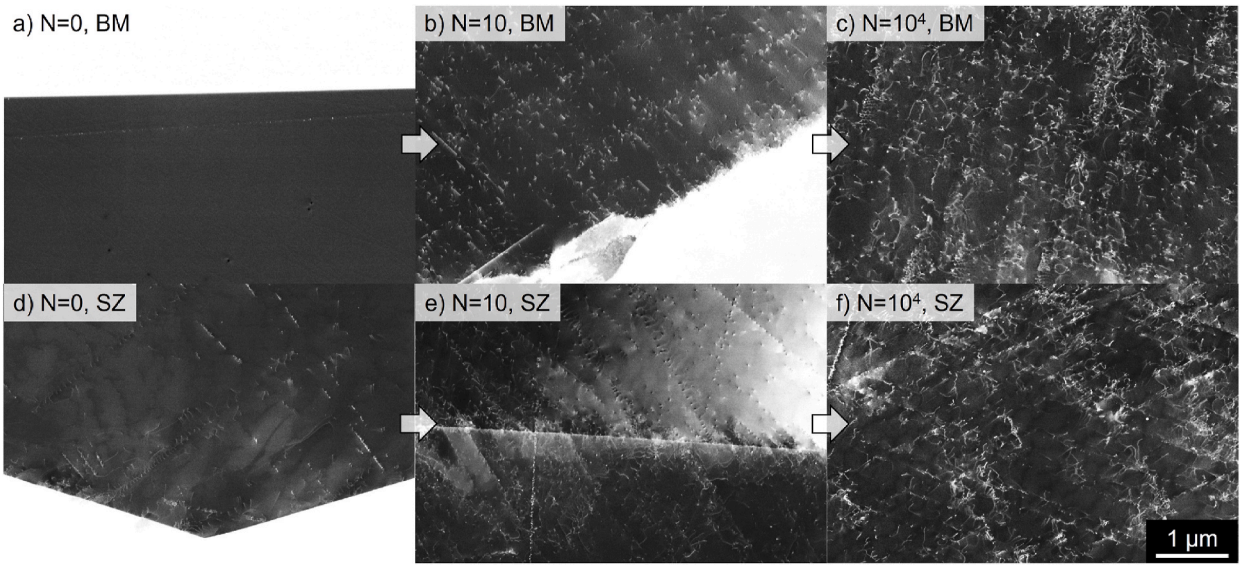

Fig. 12. – Typical change of dislocation structure by means of electron channelling contrast imaging (ECCI) in a), b), c) for the base material (BM) and in d), e), f) for the solidification zone (SZ) after different load cycles (N) at $\sigma_{max} = 440$ MPa.

dislocation walls will form [41,42].

The evolution of the dislocation structure can be linked to the measured temperature independent electrical resistivity of the austenite $\rho_{D,\ Austenite}$, shown in Fig. 10 b). During the first cycles, severe plastic deformation occurs due to cyclic creeping, causing the dislocation density to increase significantly, resulting in a rapid increase of $\rho_{D,\ Austenite}$. If no martensite correction factor for the low values is applied during the martensite measurement, $\rho_{D,\ Austenite}$ subsequently drops. But since a high correction factor seems reasonable, a short final phase of stagnation can be observed. This is probably due to interaction between dislocation migration (which may reduce resistance) and dislocation formation (which may increase resistance). This tendency can be seen in Fig. 12 b) and e). This is followed by a phase of increasing resistance up to 10^4 cycles, which is attributed to the increasing cluster formation, with increasingly limited possibility for dislocation migration. Since dislocation mobility is an important factor for cyclic creeping, this would also explain the reduced increase in the measured length L and the reduced decrease in the diameter d from this point onwards. After 10^4 cycles, the resistance stagnates regardless of whether and which correction factor was used for the martensite content. Again, dislocation formation and migration could influence each other and prevent the resistance from increasing, whereby the formation of micropores could also play a role. Only shortly before fracture does the resistance begin to increase sharply, which is associated with crack initiation and propagation, which greatly reduces the cross-section of the specimen and could not be detected with the optical micrometer.

3.4. Comparison of the influences of geometry, temperature and martensite on the electrical resistance

The various in-situ measurement systems were used to calculate the geometric, thermal and martensitic percentage changes in electrical resistance during fatigue, relative to the initial resistance, see Fig. 13. The comparison shows that the geometry has the highest influence to the electrical resistance, due to cyclic creeping or so called ratcheting [43]. The influence of temperature is small compared to the geometric influences, but at about 2 %, it is of a magnitude that should not be neglected. Similarly, the influence of martensite content is also negligible. The percentage distribution of the various influences is highly dependent on the material used and the level of stress, and therefore cannot be transferred to other materials and stresses.

This investigation demonstrates that electrical resistance alone is inadequate for making statements about microstructural changes, as a significant portion of the influences on the electrical resistance can be attributed to factors such as geometry, temperature, and martensite transformation.

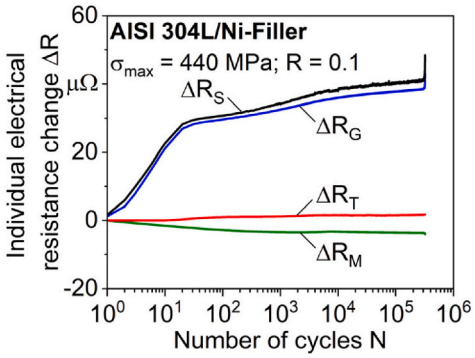

Fig. 13. – Influence comparison by geometric ΔR_G, thermal ΔR_T, and martensitic ΔR_M resistance changes during fatigue.

4. Conclusions and outlook

This study presents a method for the estimation of the evolution of microstructural changes during the fatigue testing with cyclic creeping. Various in-situ measurements were employed in a complex experimental setup to determine the electrical resistance, geometry, and temperature of the specimen. This approach allowed the compensation of the effects of geometry and temperature on the electrical resistance.

To combine strain and voltage measurement a newly developed contacting method was used. This method offers the advantage of directly transferring the measured strain to the length change of the electrical resistance measurement. Furthermore, this method allows the implementation of a voltage drop measurement in the test area, without interference from welded or soldered contacts. A comparison with fixed laser welded connections demonstrates that the newly developed contact, without a fixed connection, enables reliable measurement of the electric resistance.

During the fatigue test, a significant increase in the electrical resistance was observed, which was mostly attributed to geometric

influences. In order to determine the microstructural changes during the fatigue test, the temperature independent electrical resistivity of the austenite was calculated from the electrical resistance, taking into account the geometry, temperature, and martensite transformation influences.

It could be shown that the resistivity of the austenite can be divided into characteristic phases during creep fatigue. These phases are characterized by high deformation at the beginning and strain hardening in the following. On a microstructural level, the development of resistivity is related to the dislocation density and structure can thus provide valuable insights for interpretation.

Future investigations will focus on the transfer of this method to other materials and loading conditions and on the quantification on the different microstructural damage mechanism. Through the use of complex investigation like focused-ion-beam based 3D-volume reconstruction, scanning transmission electron microscopy (STEM) or specific heat treatments with subsequent resistance measurements, the individual influence of dislocations, voids or microcracks on the electrical resistance during fatigue will be separate.

Data availability

All raw/processed data required to reproduce these findings are available from the authors upon reasonable requests.

Declaration of competing interest

The authors declare the following financial interests/personal relationships which may be considered as potential competing interests: Lukas Maximilian Sauer has patent Sensor zur kombinierten Messung von Dehnung und elektrischem Widerstand issued to DE 20 2024 001 595.5. If there are other authors, they declare that they have no known competing financial interests or personal relationships that could have appeared to influence the work reported in this paper.

Acknowledgment

The authors gratefully acknowledge the funding by the German Research Foundation (Deutsche Forschungsgemeinschaft, DFG) for the project “Alloying- and microstructure-based fatigue life characterisation and prediction of vacuum brazed AISI 304L/NiFeCrSiB joints in corrosive environments” (project no. 408904168), the subproject B01 within the Collaborative Research Center CRC/Transregio 188 “Damage controlled forming processes” (project no. 278868966) and the project “Quantified evaluation of the influence of testing frequency on the fatigue behaviour of unalloyed steels for implementation in resource-efficient fatigue life prediction methods” (project no. 518776466).

Furthermore, the authors further gratefully acknowledge the German Research Foundation and the Ministry of Culture and Science of North Rhine-Westphalia (Ministerium fuer Kultur und Wissenschaft des Landes Nordrhein-Westfalen, MKW NRW) for financial support within the Major Research Instrumentation Program for the high-speed thermography system (project no. 444290516).

References

[1] Sorger LS, Oliveira JP, Inácio PL, Enzinger N, Vilaca P, Miranda RM, Santos TG. Non-destructive microstructural analysis by electrical conductivity: comparison with hardness measurements in different materials. J Mater Sci Technol 2019;35:360–8. https://doi.org/10.1016/j.jmst.2018.09.047.

[2] Popovic M, Romhanji E. Characterization of microstructural changes in an Al-6.8 wt.% Mg alloy by electrical resistivity measurements. Mater Sci Eng, A 2008;492(1–2):460–7. https://doi.org/10.1016/j.msea.2008.04.001.

[3] Khodabakhshi E, Simchim A. The role of microstructural features on the electrical resistivity and mechanical properties of powder metallurgy Al-SiC-Al2O3 nanocomposites. Mater Des 2017;130:26–36. https://doi.org/10.1016/j.matdes.2017.05.047.

[4] Polák J. Electrical resistivity of cyclically deformed copper. Czech J Phys B 1969;19:315–22. https://doi.org/10.1007/BF01712868.

[5] Kocer M, Sachslehner F, Müller M, Schafler E, Zehetbauer M. Measurement of dislocation density by residual electrical resistivity. Mater Sci Forum 1996;210:133–40. 10.4028/www.scientific.net/MSF.210-213.133.

[6] Hakamada M, Kuromura T, Chen Y, Kusuda H, Mabuchi M. Influence of porosity and pore size on electrical resistivity of porous aluminum produced by spacer method. Mater Trans 2007;48(1):32–6. https://doi.org/10.2320/matertrans.48.32.

[7] Koch A, Bonhage M, Teschke M, Lücker L, Behrens BA, Walther F. Electrical resistance-based fatigue assessment and capability prediction of extrudates from recycled field-assisted sintered EN AW-6082 aluminium chips. Mater Char 2020;169:110644. https://doi.org/10.1016/j.matchar.2020.110644.

[8] Li Y, Lin J, Zhao Z. Phase field study on the grain size dependent electrical resistivity-strain response in superelastic nanocrystalline NiTi alloys. J Mater Res Technol 2024;32:4092–105. https://doi.org/10.1016/j.jmrt.2024.08.215.

[9] Bishara H, Lee S, Brink T, Ghidelli M, Dehm G. Understanding grain boundary electrical resistivity in Cu: the effect of boundary structure. ACS Nano 2021;15:16607–15. https://doi.org/10.1021/acsnano.1c06367.

[10] Mohanty ON, Bhagat AN. Electrical resistivity and phase transformation in steels. Mater Werkst 2003;34(1):5–180. https://doi.org/10.1002/mawe.200390024.

[11] Gangloff RP, Slavik DC, Piasclik RS, van Stone RH. Direct current electrical potential measurement of the growth of small cracks. ASTM International; 1992. https://doi.org/10.1520/STP1149-EB.

[12] F. Walther, D. Eifler, Short-time procedure for the determination of woehler and fatigue life curves using mechanical, thermal and electrical data,Journal of Solid Mechanics and Materials Engineering 2 (4) 507–518, https://doi.org/10.1299/jmmp.2.507.

[13] Starke P, Klein M, Eifler D. Resistivity – a characteristic fingerprint of fatigue induced changes in the microstructure of metallic materials. Procedia Eng 2011;10:698–703. https://doi.org/10.1016/j.proeng.2011.04.116.

[14] Starke P, Walther F, Eifler D. Model-based correlation between change of electrical resistance and change of dislocation density of fatigued-loaded ICE R7 wheel steel specimens. Mater Test 2018;60:7–8. https://doi.org/10.3139/120.111202.

[15] Sun B, Guo Y. High-cycle fatigue damage measurement based on electrical resistance change considering variable electrical resistivity and uneven damage. Int J Fatig 2004;26:457–62. https://doi.org/10.1016/j.ijfatigue.2003.10.004.

[16] Mrzljak S, Trautmann M, Blickling P, Wagner G, Walther F. Fatigue condition monitoring of notched thermoplastic-based hybrid fiber metal laminates using electrical resistance measurement and digital image correlation. J Compos Mater 2023;57(17):2669–87. https://doi.org/10.1177/00219983231176257.

[17] Lücker L, Lingnau LA, Walther F. Non-destructive direct current potential drop assessment of forming-induced pre-damage in AISI 5115 steel. Procedia Struct Integr 2022;42:368–73. https://doi.org/10.3390/ma17123023.

[18] Singh Y. Electrical resistivity measurements: a review. Int J Mod Phys 2013;22:745–56. https://doi.org/10.1142/S2010194513010970.

[19] Matthiessen A, Bose M. On the influence of temperature on the electric conducting power of metals. Phil Trans Roy Soc Lond 1862;152:1–27. https://doi.org/10.1098/rstl.1862.0001.

[20] Reif-Acherman S. Studies on the temperature dependence of electric conductivity for metals in the Nineteenth Century: a neglected chapter in the history of superconductivity. Rev Bras Ensino Física 2011;33(4). https://doi.org/10.1590/S1806-11172011000400020. 4602–4302.

[21] Omari MA, Sevostianov I. Evaluation of the growth of dislocation density in fatigue loading process via electrical resistance measurements. Int J Fract 2013;179:229–35. https://doi.org/10.1007/s10704-012-9780-5.

[22] Lou Y, Song X, Hu S, Fu W, Chen X, Cao J. Evaluation of mechanical properties and vacuum brazing for TiAl/GH3536 hetro-honeycomb sandwich ultrathin-walled structure. Weld World 2022;66:1999–2015. https://doi.org/10.1007/s40194-022-01319-z.

[23] Boretius M. The Potential of vacuum brazing–state of the art and developments from the perspective of a service contractor. Advanced Engineering Mateirals 2006:158–61. https://doi.org/10.1002/adem.200500247.

[24] Way M, Willingham J, Goodall R. Brazing filler metals. Int Mater Rev 2020;65:257–85. https://doi.org/10.1080/09506608.2019.1613311.

[25] Penyaz MA, Ivannikov AA, Sevryukov ON, Kalin BA. Overview of nickel-based filler metals for brazing of austenitic stainless steels. Nonferrous Met 2021;1:41–56. https://doi.org/10.17580/nfm.2021.01.06.

[26] Ma H, Duan P, Liao P, Zhou G, Tu S. Effect of temperature on metallurgical reactions and microstructure evolution of 316L/BNi-2 Brazed Joints. J Mater Eng Perform 2021;31:1631–41. https://doi.org/10.1007/s11665-021-06296-w.

[27] Otto JL, Penyaz M, Schmiedt-Kalenborn A, Knyazeva M, Ivannikov A, Kalin B, Walther F. Effect of phase formation due to holding time of vacuum brazed AISI 304L/NiCrSiB joints on corrosion fatigue properties. J Mater Res Technol 2020;9(5):10550–8. https://doi.org/10.1016/j.jmrt.2020.07.047.

[28] Zhang X, Wang J, Xu Q, Liu K, Qin G. Microstructure evolution and shear strength in CoCrFeNi/AISI 304 joint by vacuum brazing with BNi-2 filler metal. J Mater Res Technol 2024;33:8425–34. https://doi.org/10.1016/j.jmrt.2024.11.176.

[29] Otto JL, Penyaz M, Möhring K, Gerdes L, Schaum T, Ivannikov A, Schmied-Kalenborn A, Kalin B, Walther F. Microstructure, residual stresses, and strain-rate-dependent deformation and fracture behavior of AISI 304L joints brazed with NiCrSiB filler metals. Metals 2021;11(4):593. https://doi.org/10.3390/met11040593.

[30] Otto JL, Sauer LM, Brink M, Schaum T, Lingnau LA, Macias Barrientos M, Walther F. A 2D and 3D segmentation-based microstructure study on the role of brittle phases in diffusion brazed AISI 304L/NiCrSiFeMoB joints. Mater Des 2023;235:112401. https://doi.org/10.1016/j.matdes.2023.112401.

[31] Sauer LM, Otto JL, Walther F. Sensor zur kombinierten Messung von Dehnung und elektrischem Widerstand (DE 20 2024 001 595.5). Deutsches Marken- und Patentamt 2024. https://register.dpma.de/DPMAregister/pat/register?AKZ=20240015955.
[32] Bayerlein M, Christ HJ, Mughrabi H. Plasticity-induced martensitic transformation during cyclic deformation of AISI 304L stainless steel. Mater Sci Eng, A 1989;114. https://doi.org/10.1016/0921-5093(89)90871-X. L22–L16.
[33] Chu TK, Ho CY. Thermal conductivity and electrical resistivity of eight selected AISI stainless steels. In: Mirkovich VV, editor. Thermal conductivity 15. Boston, MA: Springer; 1978. https://doi.org/10.1007/978-1-4615-9083-5_12.
[34] Ionescu LG, Pantawane MV, Tănase C, Sichim RV, Dascălu CA, Ghiban B. Evaluation of retained austenite in carburized bearing steel using magneto-inductive method. Crystals 2023;13(8):1173. https://doi.org/10.3390/cryst13081173.
[35] Nellessen J, Sandlöbes S, Raabe D. Effects of strain amplitude, cycle number and orientation on low cycle fatigue microstructures in austenitic stainless steel studied by electron channeling contrast imaging. Acta Mater 2015;87:86–99. https://doi.org/10.1007/s11837-013-0678-0.
[36] Moody LC, Powell IJ, Lewis DO, Johnson MC, Butler BG, Paramore JD. Cross-sectional area measurement by optical and electrical resistance methods for subscale mechanical testing of near-net-shape titanium components. Int J Refract Metals Hard Mater 2020;92:105265. https://doi.org/10.1016/j.ijrmhm.2020.105265.
[37] Uranaka S, Nishimura C, Hirashima I, Maeda T, Masumura T, Tsuchiyama T, Kawamoto Y, Shirahata H, Uemori R. Dependence of solute carbon concentration on electrical resistivity of retained austenite. Scripta Mater 2022;218:114791. https://doi.org/10.1016/j.scriptamat.2022.114791.
[38] Reynolds JA, Hough JM. Formulae for eielectric constant of mixtures. Proc Phys Soc B 1957;70(8):769–75. https://doi.org/10.1088/0370-1301/70/8/306.
[39] Ho CY, Ackerman MW, Wu KY, Havill TN, Bogaard RH, Matula RA, Oh SG, James HM. Electrical resistivity of ten selected binary alloy systems. J Phys Chem Ref Data 1983;12(2):183–322. https://doi.org/10.1063/1.555684.
[40] Gutierrez-Urrutia I, Zaefferer S, Raabe D. Coupling of electron channeling with EBSD: toward the quantitative characterization of deformation structures in the SEM. JOM 2013;65:1229–36. https://doi.org/10.1007/s11837-013-0678-0.
[41] Gerland M, Mendez J, Violan P, Ait Saadi B. Evolution of dislocation structures and cyclic behaviour of a 316L type austenitic stainless steel cycled in vacuo at room temperature. Mater Sci Eng 1990;118:83–95. https://doi.org/10.1016/0921-5093(89)90060-9.
[42] Pham MS, Holdsworth SR. Dynamic strain ageing of AISI 316L during cyclic loading at 300°C: mechanism, evolution, and its effects. Mater Sci Eng 2012;556:122–33. https://doi.org/10.1016/j.msea.2012.06.067.
[43] Paul SK. A critical review of experimental aspects in ratcheting fatigue: microstructure to specimen to component. J Mater Res Technol 2019;8(5):4894–914. https://doi.org/10.1016/j.jmrt.2019.06.014.